

Reverse Engineering of Multifocal Intraocular Lenses Using a Confocal Microscope

Damian Mendroch
 Institut für Angewandte Optik
 Technische Hochschule Köln
 Köln, Deutschland
 damian.mendroch@smail.th-koeln.de

Abstract—This paper presents a method for reverse engineering multifocal intraocular lenses using a standard confocal microscope and dedicated processing in Python. Methods for stitching of elevation data, centering and alignment of the lens are implemented in software, as well as filtering methods and algorithms that allow to determine the mathematical description of the aspherical base part of the lens. Measurement and processing was conducted on three different lenses, the results include all needed geometrical information to create a full three dimensional lens model for further analysis.

Index Terms—multifocal intraocular lens, confocal microscopy, lens metrology, aspheric surface, fitting, reverse engineering

I. INTRODUCTION

Despite an ever-growing trend in cataract surgeries and evermore technological advancements in intraocular lens design and surgery standards, monofocal lenses are still the main type implanted in those procedures [1, 2]. In contrast to multifocal intraocular lenses (MIOL), the issue with monofocal lenses is the patients still needing optical aids for sharp vision at different distances. MIOLs allow for multiple focal lengths and can implement far, near and intermediate vision, but are more complicated optically by using different viewing zones and incorporating different optical effects like refraction and diffraction. With the manufacturers keeping the exact design of the MIOL a trade secret, there are no models of these lenses available. Such lens models would allow for a full understanding of the design decisions and enable research on issues and possibilities more easily.

The aim of this research work is the reverse engineering of three different multifocal intraocular lenses. Contrary to typical aspherical surface measurement methods, like interferometry or profilometers [3], the measurements were conducted using a conventional confocal microscope.

II. MULTIFOCAL INTRAOCULAR LENSES

A. Functioning principle

Multifocal intraocular lenses can be of refractive multizone design or use a refractive-diffractive design, here we will focus on the latter case. Additionally to the refractive base lens design a diffractive ring structure is added, which adds one or multiple focal points. The structure height lies typically in the range of the wavelength to a few microns. Although such a profile, like shown in figure 1, resembles a fresnel lens at

first glance, the structure is dimensioned in such a way that the light is not only bend to the focus, but also only interferes constructively at the focal point [4]. Using variations of height and width in the profile, the number of focal points, the light distribution ratio between them as well as the optical powers can be controlled [5]. Additional design decisions include different viewing zones, depending on the field of view or the pupil size, and the reduction of typical lens aberrations as well as glares and halos, which can be prominent in MIOLs because of the overlap of multiple differently focussed images on the retina [6].

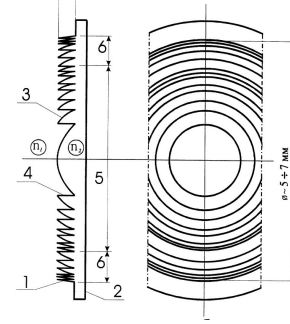


Fig. 1. Exemplary diffractive profile [7].

B. Aspherical Surfaces

The base form of a typical MIOL is an asphere. The typical mathematical formulation for such an asphere is specified by the DIN ISO 10110 [8]:

$$z(r) = \underbrace{\frac{\rho r^2}{1 + \sqrt{1 - (1 + k)(\rho r)^2}}}_{\text{Conic Section}} + \underbrace{\sum_{i=2}^n A_{2i} \cdot r^{2i}}_{\text{higher order even polynomial}} \quad (1)$$

$z(r)$	sag
r	distance to optical axis
ρ	curvature constant
k	conic constant
A_{2i}	polynomial coefficients

The conic sections component reduces or eliminates the spherical aberration with ρ defining the curvature near the optical axis and therefore the optical power, k describes which conic

section form the curve takes, which is dependent on the refraction indices of the media. Examples for conic sections can be found in figure 2.

The polynomials enable additional degrees of freedom with which other aberrations can be reduced, the calculation of A_{2i} depends highly on the use case and is done using simulation software. The DIN ISO 10110 standard also includes odd polynomials, but they were excluded here because of their rare usage.

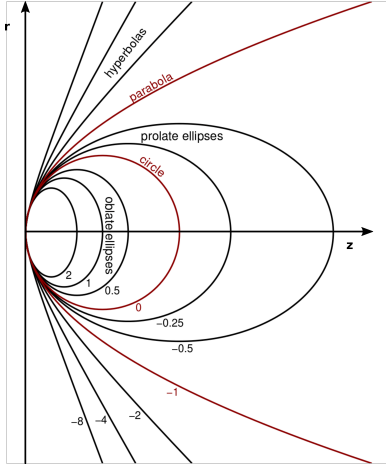


Fig. 2. Conic sections for a constant ρ and a varying k [9].

III. MEASUREMENT

All elevation measurements were conducted using the μ surf custom confocal microscope from nanofocus. Contrary to the typical opaque and diffusely reflecting measurement object, some measurement parameters need to be adapted to allow for correct data acquisition. Due to a small reflectivity of the lens surface, the illumination as well as the camera's exposure time need to be set significantly higher. In consequence of the mostly specular reflection the maximum measurable slope angle is dependent on the numerical aperture of the objective. The 800-S (20x) objective allows only for slope angles up to 13.7° and could only be used for lenses with low curvature like the SN6AD1, for the MS612 and ZMA00 lens measurement the 320-S (50x) objective had to be used, which allows for angles up to 26.6° .

The microscope measurement range is smaller than the lens, so multiple images need to be taken and stitched together. With the assumption of rotational symmetry a radial measurement from lens axis to outer edge is sufficient. Nevertheless, lens images from one edge to the other were conducted in this paper to acquire redundant data for better processing and to estimate measurement uncertainties.

The sample is positioned on a tilt platform that allows for three-axis angular orientation. With the help of a test measurement and the microscope software we can determine the lens tilt using reference points like the diffractive steps. This can be seen in figure 3. The tilt values can be translated to a micrometer screw setting that fully compensate the tilt.

In practice a low value of below 0.1° still persists, but can be compensated using the procedure in section VI-C.

The measurement data has a resolution in x and y direction of $0.625\mu\text{m}$ for the 320-S (50x) and $1.5625\mu\text{m}$ for the 800-S (20x) objective. The effective resolution in z -direction is harder to quantify, because it depends on noise and the measurement settings, but can be below of $0.1\mu\text{m}$.

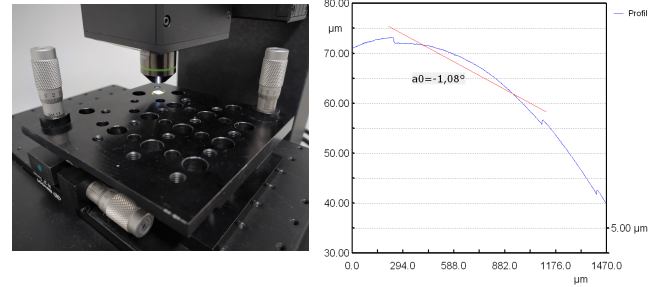


Fig. 3. Tilt platform (left) and tilt measurement in the μ soft software (right).

IV. PROCESSING PROCEDURE

For the creation of a three dimensional lens model the geometrical surface information of both sides as well as the distance between the surfaces are needed. Additionally the refraction index has to be specified, it can be found using manufacturer data. The distance between the surfaces is measured taking an image of the lens edge and measuring the edge thickness.

The steps needed to measure both surfaces are more numerous, consisting of

- 1) importing the data into python
- 2) stitching the subimages if needed
- 3) interpolating missing data inside the lens
- 4) specifying geometrical properties of the lens (axis position, lens diameter)
- 5) detecting and compensating the lens tilt
- 6) calculating the lens profiles
- 7) interpolating lens profiles
- 8) filtering the profiles
- 9) exporting the processed data and processing settings

All processing is implemented in Python, the code can be found in [10].

V. STITCHING

A. Task

The displacement between the individual images is done using a stepper motor. But with the stepper motor being an open loop system, there is no precise feedback on the absolute motor position and the shift values between the images in x , y and z direction. The typical image position uncertainty lies in the order of magnitude of $1 - 10\mu\text{m}$. With the help of overlapping image regions and methods for shift detection, the shift vectors can be estimated. The used method of the microscope software is described in V-B and works well for data with surface variations and details, but is

problematic for flat surfaces with few details like the mostly plain lenses. Here the algorithm finds a high correlation for many possible shifts or in the extreme case no statements can be made at all about the correct shift value. Noise in the measurements and a not completely corrected distortion and field curvature of the objective complicate the shift detection further. The results are shift errors between individual images, with measurements consisting of 10 or even 20 subimages the errors can add up very unfavorably. Resulting shift errors were visible throughout most measurements and have worsened the data quality drastically.

The idea is to implement additional shift detection methods to improve the detection and adapt the stitching to our needs. The following methods only describe a shift detection in x and y direction, the shift in z direction is calculated using the median difference of both overlapping regions.

B. Microscope Stitching Method

The microscope features multiple stitching modes, with each having different methods that are attempted in a specific order. The standard mode consists of [11]:

- 1) try using the intensity data for correlation
- 2) if this fails, try using the height data
- 3) if this also fails, assume precise motor position

Unlike the other following methods, this one was not implemented in the project, since it is already featured in the microscope software.

C. No Shift Detection Mode

This stitching method assumes precise motor position and overlays the pictures without additional shift detection.

D. Fourier Transform Shift Detection

This method obtains the image shift using the shift theorem of the Fourier transformation. The height functions in the overlapping region are

$$\begin{aligned} h_1(x, y) \\ h_2(x, y) \approx h_1(x - s_x, y - s_y) \end{aligned} \quad (2)$$

with the assumption, that the second one is the first shifted by a vector $\vec{s} = (s_x, s_y)$. Transforming to the Fourier domain yields:

$$\begin{aligned} H_1(f_x, f_y) &= \mathcal{F}\{h_1(x, y)\} \\ H_2(f_x, f_y) &= \mathcal{F}\{h_2(x, y)\} \approx H_1(f_x, f_y) \cdot e^{-i2\pi(f_x s_x + f_y s_y)} \end{aligned} \quad (3)$$

The exponential function can be isolated using the ratio

$$Q = \frac{H_2(f_x, f_y)}{H_1(f_x, f_y)} \approx e^{-i2\pi(f_x s_x + f_y s_y)} \quad (4)$$

Inverse transformation yields a dirac pulse at the shift position.

$$V = \mathcal{F}^{-1}\{Q\} \approx \delta(x - s_x, y - s_y) \quad (5)$$

Finding the maximum in the data obtains the position of the dirac pulse and therefore the shift vector \vec{s} . In practice the assumption $h_2(x, y) \approx h_1(x - s_x, y - s_y)$ does not always hold true because of noise and some information being only

present in one of the pictures. To exclude these sub-optimal cases two additional criteria were added. First, the shift vector is only valid, if it lies within a realistic shift region of $50 \times 50 \mu\text{m}$. Second, only use the shift vector if the maximum is distinctive enough, mathematically formulated by being an outlier 6σ above the mean.

E. Variance Minimization Shift Detection

When using the difference $h_2 - h_1$ we assume that this difference has its smallest overall variance at the correct shift value. The variance, being nothing different, than the mean quadratic deviation from mean value, is defined as

$$\sigma^2 = \frac{1}{n} \sum_{i=1}^n (x_i - \mu)^2 \quad (6)$$

with n being the sample size, μ the mean value and x_i the value of the data points. Calculating the variances for a set of possible shifts a variance map $V(s_x, s_y)$ is obtained from which we can choose the shift with the smallest variance as optimal shift vector \vec{s} . Same as with the Fourier transform shift detection, the assumption $h_2(x, y) \approx h_1(x - s_x, y - s_y)$ does not always hold true, so we use the same criteria, only using shift values when withing a specific region and only if the minimum is distinctive enough.

F. Results

In figure 4 you can find varying results for a measurement using different stitching methods. Depending on the method, the variance in the profile data is reduced and the relative position of the diffractive zones matches more properly. However, there is no universal superior method that performs better than the others. Instead, we know have the possibility and flexibility to decide which method to use for each measurement. Unfortunately, in some measurements stitching errors are still noticeable independent of the method applied.

VI. PROCESSING

A. Interpolation of Missing Data

After the measurement there is initially some missing data inside of the lens. Causes are regions out of focus or with a too steep slope angle. Because of missing values we have no gridded data anymore, so methods for ungridded interpolation have to be used, but these are slow (around 30s) on datasets with several millions of datapoints. Instead we apply line- and column-wise one dimensional interpolation on the image and use the average of both methods for each missing data point. This procedure produces slightly worse results than the full two dimensional interpolation, but it reduces processing time to the sub-second range. Since the data is averaged and filtered in following steps anyway, a few slightly incorrect datapoints should have mostly no impact.

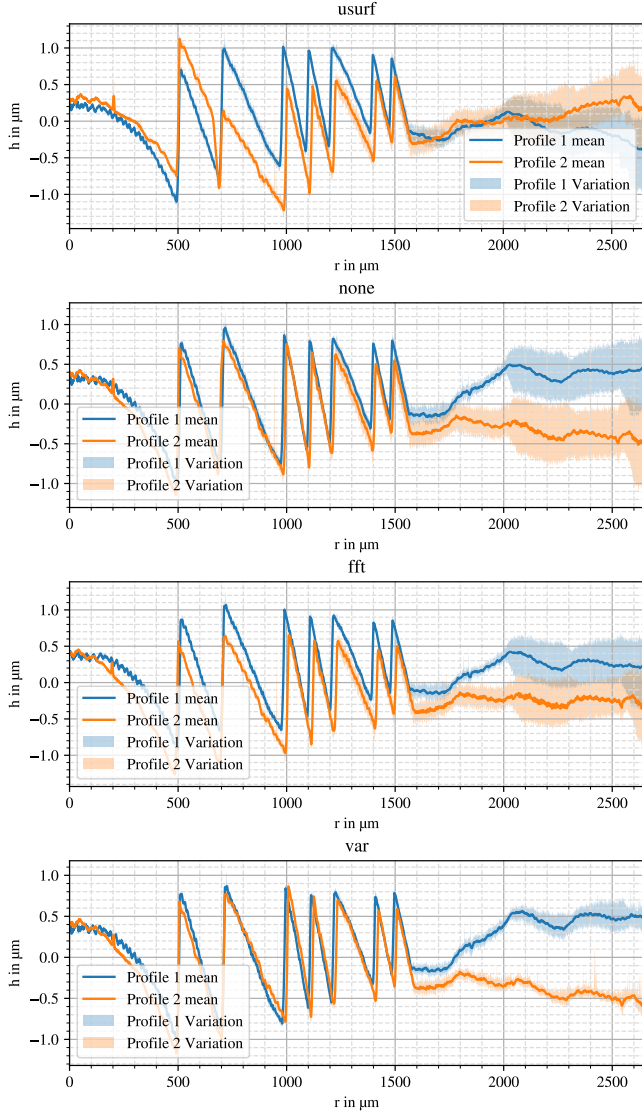


Fig. 4. Different stitching results depending on the methods microscope stitching, no shift detection, fourier detection and variance minimization (from top to bottom).

B. Centering and Cropping

Finding the lens axis and edge creates some larger challenges. Due to the uncompensated tilt and noise the axis is not implicitly at the maximum of the surface, and the edge of valid data is not implicitly the edge of the lens. Due to stitching errors even the centers of the diffraction rings don't overlap at the lens axis in all cases. To reduce processing and program complexity, the solution in the processing script includes the user specifying the axis and edge using a suitable plot. Using a nonlinear sigmoid function on the surface derivative, like shown in equation 8, we use the range compression to normalize outliers and make small changes in the gradient visible. For comparable results between measurements and objects the gradient is first normalized at its 0.65 quantile.

The gradient magnitudes are defined as

$$\begin{aligned} G_1 &= |\nabla z| \\ G_2 &= |\nabla G_1| \end{aligned} \quad (7)$$

With the help of a sigmoid function we obtain the compressed first and second gradient using the normalized gradients G_{1p65} and G_{2p65}

$$\begin{aligned} G_{1N} &= \frac{G_1}{\sqrt{G_1^2 + G_{1p65}^2}} \\ G_{2N} &= \frac{G_2}{\sqrt{G_2^2 + G_{2p65}^2}} \end{aligned} \quad (8)$$

An example for a compressed gradient plot can be found in figure 5. An "x" and two circles help the user overlay the lens axis, edge and a diffraction ring with the data.

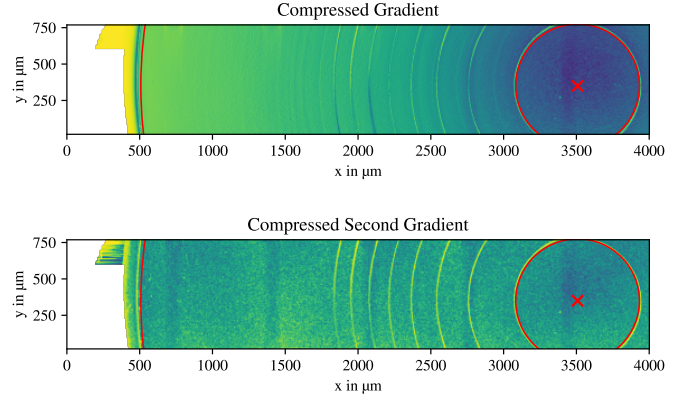


Fig. 5. First and second compressed gradient. The red circles and the "x" are visual aids.

C. Alignment

A two axis rotation around the lens axis point can be described using two rotation matrices:

$$R_x(\alpha) = \begin{pmatrix} 1 & 0 & 0 \\ 0 & \cos \alpha & -\sin \alpha \\ 0 & \sin \alpha & \cos \alpha \end{pmatrix} \quad (9)$$

$$R_y(\beta) = \begin{pmatrix} \cos \beta & 0 & \sin \beta \\ 0 & 1 & 0 \\ -\sin \beta & 0 & \cos \beta \end{pmatrix} \quad (10)$$

$R_x(\alpha)$ rotates around the x-axis and $R_y(\beta)$ around the y-axis, respectively. Assuming that the remaining tilt is rather small, since we compensated most of it using the tilt platform procedure in section III, for small α and β the cosine terms can be simplified to 1. Another assumption is that the change in z direction is rather small compared to the x and y dimensions, so we can neglect the change in x and y direction due to rotation. Using this, we get simplified terms for the rotation matrices:

$$R_x(\alpha) = \begin{pmatrix} 1 & 0 & 0 \\ 0 & 1 & 0 \\ 0 & \sin \alpha & 1 \end{pmatrix} \quad (11)$$

$$R_y(\beta) = \begin{pmatrix} 1 & 0 & 0 \\ 0 & 1 & 0 \\ -\sin \beta & 0 & 1 \end{pmatrix} \quad (12)$$

The change in z due to lens tilt breaks down to

$$\Delta z = -x \cdot \sin \beta + y \cdot \sin \alpha \quad (13)$$

We now have two independent terms for α and β . For a rotational symmetric lens we also have axial symmetry around the x and y -axis. In the tilted cases the left side of the y axis and the right side differ by $2 \cdot (-x \cdot \sin \beta)$, while the upper and lower part differ by $2 \cdot (y \cdot \sin \alpha)$ due to equation 13. Subtracting these sides from each other and determining the slope using linear regression we can estimate α and β .

D. Profile Generation

In this step the radial profiles are created, going from the lens axis to the outer edge of the lens. At this point the tilt compensation using equations VI-C and 12 takes place. In the following steps we operate not on the 2D height data but on the 1D profiles only.

E. Decomposition

With the help of the considerations from section II-B, we assume that the lens profile $MIOL$ consists of the parts cone section CS , polynomial part PR and diffraction profile DP

$$MIOL = CS + PR + DP \quad (14)$$

The conic section is the main part, while the diffraction profile is the minor one. The polynomials are only noticeable at the edges because of the r^n behavior. It is also assumed that the diffraction profile contains mainly high frequency components that don't add up to the other parts. The cone section is calculated using a conic section regression on the inner part of the lens, where the polynomial part is negligible. Conventional methods like gradient descent need suitable starting parameter, depending on the problem large computation times and it is not guaranteed, that we don't converge into a local minimum. Therefore a different approach with parameter substitution and solving an overdetermined linear equation systems was used, the exact mathematical description would exceed the scope of this paper, but can be found in the code documentation in [10].

Using this conic section regression we can determine ρ , k as well as an height offset z_0 that is added to the conic section. The polynomial part is calculated by doing a polynomial regression (order $n = 8$) on the difference of $MIOL$ and CS . Using numpy's poly1d function the regression becomes very straightforward. However, the profile mirrored around the optical axis was added to enforce only even polynomial coefficients. The remaining part as of equation 14 is the diffraction profile.

F. Profile Interpolation

The processing script gives the user the possibility to use linear interpolation on the profile to remove remaining outliers or foreign objects in the profile.

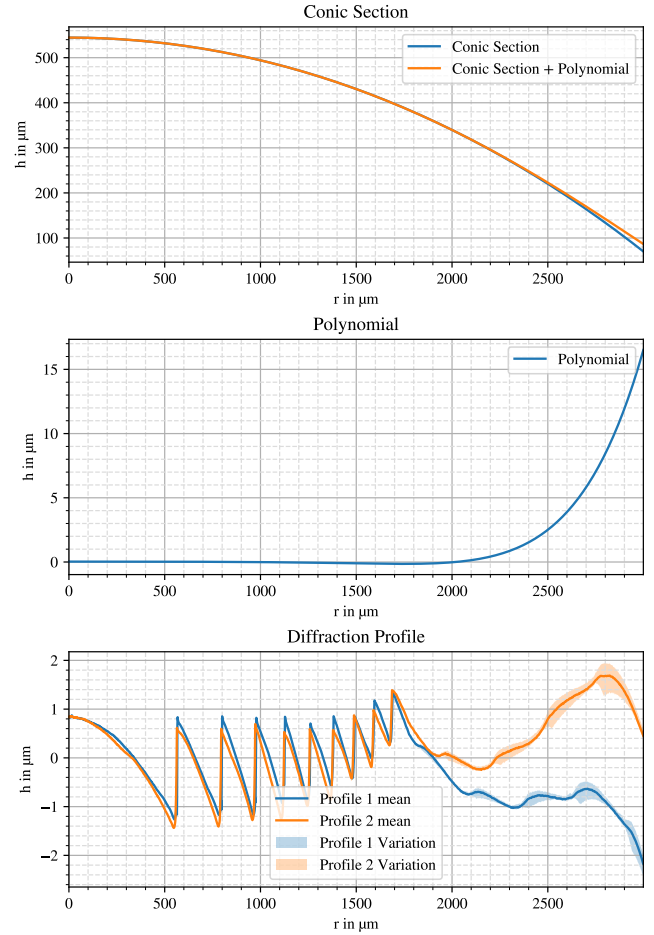


Fig. 6. Component decomposition of the MS612DAY lens.

G. Profile Filtering

Conventional smoothing also filters out sharp edges like the steps in our data. Instead a section-wise filtering using spline polynomial filtering is applied. The sections are created with the help of the absolute value of the second derivative of the profile and a threshold. The second derivative has its highest magnitude at the beginning and ending of the steps, using gaussian filtering before taking the absolute value and after derivation yields a clean pulse for every step. Utilizing a user specified threshold the sections are divided and filtered independently while the step regions are copied to the output. An example can be found in figure 7.

H. Export

In the last step all processing properties as well as the processed data are saved to a numpy archive (.npz) for further processing or analysis.

VII. RESULTS

Manufacturer data on the evaluated lenses can be found in table I. D denotes the optical power, with the first value being the base power and the second one the near addition. d_o is the optical diameter. The results of the processing can be

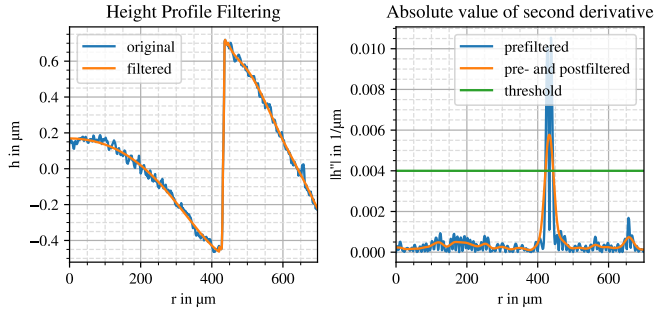


Fig. 7. Filtering example on a noisy measurement.

TABLE I
MANUFACTURER DATA ON THE EVALUATED LENSES [12].

Lens	Manu- facturer	Type	D / dpt	d_o / mm	Material
SN6AD1	Alcon	biconvex, multifocal, aspheric	13.0 +3.0	6.0	acrylic hydro- phobic
MS612 DAY	Dr. Schmidt	biconvex, multifocal, aspheric	25.5 +3.5	6.0	silicone
ZMA00	AMO	biconvex, multifocal, aspheric	30.0 +4.0	6.0	acrylic hydro- phobic

seen in table II. d_e is the edge thickness of the lens. Instead of listing all polynomial coefficient for the polynomial part, you find $q = \frac{|\Delta h_p|}{|\Delta h_c|}$ there, which is the ratio of the height change $|\Delta h_p|$ due to the polynomial and $|\Delta h_c|$ the change due to the conic section. Instead of the curvature constant ρ the more commonly curvature radius $R = \frac{1}{\rho}$ is listed there. n denotes the number of diffraction rings on the lens surfaces with a diffraction profile (Side 1 on each lens). As can be seen, the measured optical diameter d_o differs from the real value 6.0 mm, this can be due to remaining stitching errors. As expected, all lenses deviate from the spherical form $k = 0$ and polynomial parts are also prominent. The diffraction profiles for these lenses can be found in figures 8, 9, and 10. The two curves correspond to the filtered profiles left and right in the picture, a difference still persists because of stitching issues, not optimally compensated tilt or measurement uncertainties. With the deviation being in the range of a few 100 nm at the diffractive part and up to $2 \mu\text{m}$ in the refractive part of the profile, it has to be examined if the simulation results will differ depending on which curve is used for the lens model.

TABLE II
DETERMINED LENS CHARACTERISTICS.

Lens	d_e / μm	Side	d_o / mm	R / mm	k	q / %	n
SN6AD1 (13.0D)	160	1	5.994	36.14	-99.1	-	9
		2	5.984	34.18	-7.05	1.16	-
MS 612 DAY	245	1	5.998	9.985	1.14	3.51	10
		2	5.984	10.81	-1.11	0.96	-
ZMA00	215	1	5.928	14.39	-3.61	4.18	30
		2	5.689	6.539	-2.13	0.83	-

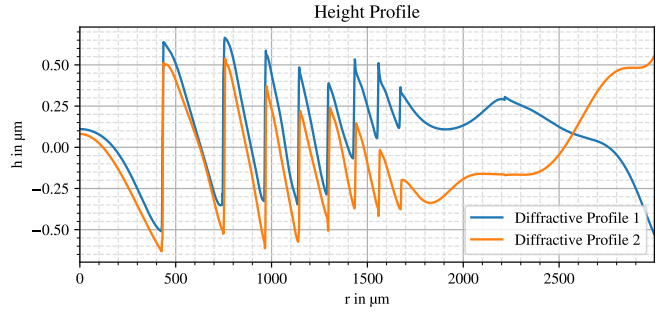


Fig. 8. Diffraction profile of the SN6AD1 lens.

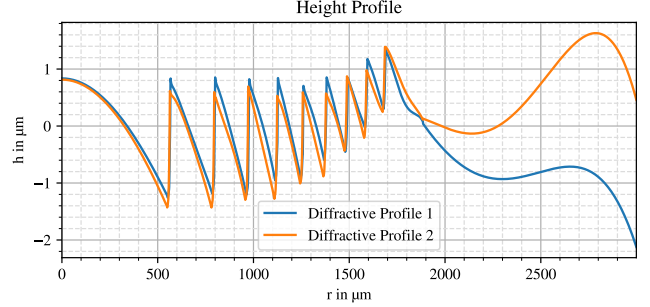


Fig. 9. Diffraction profile of the MS612DAY lens.

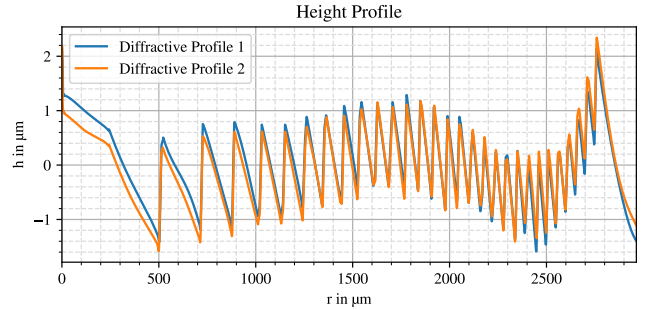


Fig. 10. Diffraction profile of the ZMA00 lens.

VIII. CONCLUSION

It has been shown, that it is possible to produce a reliable lens profile model despite inadequate centering and alignment of the lens. With the help of implemented algorithms for filtering and interpolation data quality is improved, while with a component decomposition procedure we can estimate the different parts of the lens and obtain a purely analytical description of the aspheric base lens part. However, incorrect stitching still poses some issues that are hard to eliminate and would be better solved using a measuring device with a precise motor displacement. If and how the remaining deviation in the lens profile affects the analysis of functioning principles needs to be further examined.

REFERENCES

- [1] Inkwood Research. *Global Intraocular Lens Market Forecast 2019-2027*. <https://www.inkwoodresearch.>

com/reports/global-intraocular-lens-market/, accessed 06.03.2021.

- [2] eyewire news. *Steady Growth in Cataract Surgical Procedures Is Expected Over the Next 5 Years*. <https://eyewire.news/articles/steady-growth-in-cataract-surgical-procedures-is-expected-over-the-next-5-years/>, accessed 06.03.2021.
- [3] Andreas Beutler. “Metrology for the production process of aspheric lenses”. In: *Advanced Optical Technologies, Volume 5, Issue 3*, pp.211-228 (2016).
- [4] James A Davison and Michael J Simpson. “History and development of the apodized diffractive intraocular lens”. In: *Journal of Cataract & Refractive Surgery* (2006).
- [5] Dr. Assouline. *Medicontur Bi-Flex Multifocal Presentation and Results*. https://web.archive.org/web/20181206232859/https://www.domedics.ch/fileadmin/_migrated/content_uploads/Medicontur_Bi-Flex_Multifocal_Presentation_and_Results.pdf, accessed 06.03.2021.
- [6] Liberdade C. Salerno, Mauro C. Tiveron, Jr., and Jorge L. Alio. “Multifocal intraocular lenses: Types, outcomes, complications and how to solve them”. In: *Taiwan Journal of Ophthalmology* (2017).
- [7] RussianPatents.com. *Diffractive intraocular lens*. <https://russianpatents.com/patent/218/2186417.html>, accessed 21.11.2020.
- [8] Deutsches Institut für Normung e.V. “Teil 12 Asphärische Oberflächen”. In: *DIN ISO 10110 Optik und Photonik – Erstellung von Zeichnungen für optische Elemente und Systeme* (2016).
- [9] 0x30114 at English Wikipedia. *An illustration of various conic constants*. https://commons.wikimedia.org/wiki/File:Conic_constant.svg, accessed 24.02.2021.
- [10] *miol-reng-tools github repository*. <https://github.com/drocheam/miol-reng-tools>, accessed 18.03.2021.
- [11] Nanofocus. *µsurf Dokumentation Stitching*.
- [12] IOL-info.com. *Intraokularlinsen*. <http://www.iol-info.com/intraocularlens/detail/>, accessed 06.03.2021.